Revista Virtual de Química

Article

http://dx.doi.org/10.21577/1984-6835.20250047

Anode Containing Nickel and Molybdenum Oxide Catalysts for Ethanol Reforming in Solid Oxide Fuel Cells

Ânodo Contendo Catalisadores de Óxido de Níquel e Molibdênio para Reforma de Etanol em Células a Combustível de Óxido Sólido

Welerson J. Lima,[a] Tulio Matencio,[a] Rosana Z. Domingues,[a] Thais O. Ferreira,[a] Gustavo H. M. Gomes,[c] Nelcy D. S. Mohallem[b,]*

[a]Universidade Federal de Minas Gerais, Departamento de Química, ICEx, Laboratório de Materiais e Pilhas a combustível (LaMPaC), CEP 31270-901, Belo Horizonte-MG, Brasil

[b]Universidade Federal de Minas Gerais, Departamento de Química, ICEx, Laboratório de Materiais Nanoestruturados, CEP 31270-901, Belo Horizonte-MG, Brasil

[c]Universidade Federal de Itajubá, Campus Itabira, Instituto de Ciências Puras e Aplicadas, CEP 35903-087, Itabira- MG, Brasil

***E-mail:** nelcy@ufmg.br

Submissão: 17 de Abril de 2025

Aceite: 29 de Agosto de 2025

Publicado online: 22 de Setembro de 2025

This work presents a catalytic anodic layer based on nickel and molybdenum oxides (NiO/MoOx) for ethanol reforming in solid oxide fuel cells (SOFCs). Flat disc-shaped cells (50 mm diameter, 0.4 mm thick) were fabricated, incorporating a cathode, electrolyte, and a catalytic anode containing both nickel and molybdenum oxide. Unlike most studies focusing on button cells with active areas of 0.5–1.0 cm^2, this work explores a larger active area of 9.62 cm^2, advancing efforts toward scalable SOFC designs. Electrochemical performance was assessed through impedance spectroscopy and voltammetry. At 740 °C using hydrogen, the cell without MoOx showed a polarization resistance of 0.43 Ω cm^2, a current density of 0.67 A cm for the maximum peak power density of 345.6 mW cm^{-2}. With MoOx, polarization resistance dropped to 0.33 Ω cm^2, current density increased to 0.79 A cm^{-2} for the maximum power density of 378.4 mW cm^{-2}. Using an ethanol-water (1:3) mixture, the cell with MoOx achieved superior performance: 0.23 Ω cm^2 polarization resistance, 0.97 A cm^{-2} current density for the maximum power density of 404.4 mW cm^{-2} —versus 0.28 Ω cm^2, 0.62 A cm^{-2} for 300.4 mW cm^{-2} without the catalyst. These results highlight the effective catalytic role of MoOx in enhancing SOFC efficiency during direct ethanol reforming.

Keywords: SOFC; catalytic anode; catalytic converter; molybdenum oxide; ethanol reform.

1. Introduction

The increasing scarcity of fossil fuels, the intensification of climate change, and rising emissions of greenhouse gases[1] have driven the global search for sustainable and renewable energy solutions. International agreements, such as the Paris Agreement and the United Nations Sustainable Development Goals, underscore the urgent need for technologies that can provide cleaner energy with minimal environmental impact.[2]

Solid oxide fuel cells (SOFCs) have attracted significant attention due to their high efficiency, low emissions, and flexibility in the use of various fuels. Traditionally, these cells have superior performance when powered by pure hydrogen, since the direct electrochemical reaction of hydrogen with oxygen occurs more efficiently and with lower polarization losses. However, the use of alternative fuels, such as ethanol, arouses great interest because they are renewable and environmentally friendly, despite the fact that, in general, they have lower performance compared to hydrogen. Furthermore, targeting ethanol as a fuel for SOFCs is also strategically motivated by the existing ethanol distribution infrastructure in countries like Brazil, which facilitates its use. In contrast, hydrogen lacks an established distribution network, posing significant logistical and economic challenges for widespread adoption.[3,4]

The development of materials for preparing solid oxide fuel cells (SOFCs), which directly convert chemical energy into electricity through electrochemical reactions,[5] has emerged as a promising solution due to their high efficiency, low emissions, and flexibility in fuel use.[6-9]

Solid oxide fuel cells with nickel-based anodes exhibit high electronic conductivity and excellent catalytic properties.[10] However, Ni catalysts are susceptible to deactivation by coking, which limits their application.[11] To overcome these challenges, catalysts such as molybdenum (Mo) can be incorporated into the Ni matrix, creating a substitutional solid solution Ni-Mo.[12] Introducing Mo promoted significant improvements in nickel's catalytic activities and stabilities in partial oxidation tests of isooctane. The main advantages were higher conversion and synthesis gas production. Ni-Mo surpasses monometallic catalysts such as nickel

supported on ceria-zirconia electrolyte (Ni/CZ). Another relevant factor is that monometallic nickel catalysts tend to sinter at high temperatures, reducing their surface area and catalytic activity. The presence of Mo can enhance the interaction between Ni particles and the CZ support, which can be attributed to the electrical properties of the Ni/Mo phase, as determined by density functional theory (DFT) calculations.[13] The effective interaction between Mo and Ni delays the sintering of nickel particles, preserves catalytic sites, enhances dispersion, and inhibits coke formation.[12, 13]

Various catalysts have been developed to address the challenges of carbon deposition during the internal reforming of ethanol in solid oxide fuel cells (SOFC). One notable development by Steil *et al*. involved a 600 µm thick anode-supported cell (Ni-YSZ) with a 25 µm catalytic layer (Ir/CGO) containing 0.1% by weight of the Ir catalyst, a 10 µm YSZ electrolyte, and an LSM cathode with an active area of 8 cm^2. This configuration achieved a power density of 420 mW cm^{-2} using a 10% ethanol vapor and 90% air mixture at 850 °C. Long-term tests (700 h) showed that cells without the catalyst experienced operational issues due to carbon deposition after 5 hours, while no carbon formation occurred in cells with the catalyst, demonstrating the potential of Ir for ethanol reforming in SOFCs.[14]

A SOFC composed of a YSZ support electrode, a functional anode (Ni/YSZ), and a catalytic anode (Ni/GDC) was studied by Noronha and Fonseca. Performance tests conducted at 850 °C with varying configurations yielded power densities of 50 and 40 mW cm^{-2} for hydrogen and ethanol, respectively, in the first configuration, which featured 18% nickel by weight in the catalytic layer. The second configuration (44% nickel by weight) produced power densities of 58 and 40 mW cm^{-2} with hydrogen and ethanol, respectively.[15]

Nickel catalysts supported on CeO_2 doped with different elements (Gd, Y, Pr, Zr, Nb) to minimize carbon deposition during ethanol reforming in SOFCs were explored by Silva *et al*. Among the tested catalysts, Ni/CeNb showed the least carbon formation, while the other catalysts (Ni/CeGd, Ni/CeY, Ni/CePr, and Ni/CeZr) exhibited similar levels of carbon deposition. The authors concluded that the lower carbon formation with Ni/CeNb was likely due to the presence of the $NiNb_2O_6$ phase, emphasizing the limitations of using redox supports to aid carbon removal under typical SOFC conditions.[16]

A 40 µm thick LSCF cathode was developed by Lo Faro *et al*., whose cell was tested with NiCu/CGO and NiCo/CGO bimetallic catalysts, reaching power densities of 500 and 370 mW cm^{-2}, respectively, for NiCo and NiCu using hydrogen at 800 °C. When using a 1:3 ethanol-water mixture as fuel, power densities were 275 and 210 mW cm^{-2} for NiCu and NiCo, respectively, and 550 and 340 mW cm^{-2} with pure ethanol.[11]

A button cell with a 1 mm thick Ni-GDC anode, a 22 µm GDC electrolyte, and a 25 µm LSCF-GDC cathode was produced by Zhang *et al*., achieving power densities of 1660 mW cm^{-2} using hydrogen and 1370 mW cm^{-2} using a 70% ethanol-30% N_2 mixture at 700 °C.[17]

Donazzi and collaborators also fabricated a button cell featuring a 140 µm thick ScSZ supporting electrolyte, a 3 µm samaria-doped ceria electrolyte, a 20 µm STF cathode, and a 20 µm STF-Ru anode. This cell achieved power densities of 400 mW cm^{-2} with hydrogen and 195 mW cm^{-2} with ethanol-water at 800 °C.[18]

A SOFC with a Ni/YSZ support anode and a bi-layer electrolyte composed of YSZ and GDC was developed by Liu *et al*., achieving a power density of 944.5 mW cm^{-2} at 800 °C using 6.5% ethanol.[19] Li *et al*. fabricated an electrolyte-supported fuel cell using $La_{0.9}Sr_{0.1}Ga_{0.8}Mg_{0.2}O_{3-\delta}$ (LSGM) as the electrolyte and $Ce_{0.2}Sr_{0.8}Fe_{0.95}Ni_{0.05}O_3$ as the cathode and anode, achieving a power density of 580 mW cm^{-2} at 800 °C with ethanol.[20]

Two types of button cells featuring Ni-YSZ support anodes, LSCFN-GDC cathodes and GDC/ScSZ electrolyte, were produced by Zhang *et al.* The cell with LSCFN as a catalyst achieved power densities of 2110 mW cm^{-2} with hydrogen and 970 mW cm^{-2} with ethanol at 800 °C, while the Ni-YSZ-based cell achieved 2160 mW cm^{-2} with hydrogen and 1360 mW cm^{-2} with ethanol.[21]

Rao *et al.* produced a cell with a Ni-YSZ support anode, YSZ/GDC electrolyte, and a catalytic layer of $Ni_{0.9}Cu_{0.1}TiO_{3-\delta}$, reaching power densities of 1100 and 867 mW cm^{-2} with hydrogen and ethanol, respectively, at 800 °C [22] and Elharati *et al.* developed a fuel cell using Rh/CZ as the catalytic anode, achieving power densities of 340 mW cm^{-2} with hydrated hydrogen and 260 mW cm^{-2} with an ethanol-water mixture at 600 °C.[23]

Table 1 summarizes the information from the literature review on direct fuel reforming in SOFCs. All catalysts used are formed by transition metals known for their homogeneous and heterogeneous catalytic activity, with the ability to adopt multiple oxidation states.

Despite these advancements, several research gaps remain. For instance, while MoO_x has been shown to improve catalytic activity and reduce coking in small button cells, its impact on larger SOFCs with expanded active areas, where mechanical and thermal challenges are more pronounced, remains unclear.[24] Moreover, the mechanisms by which MoO_x influences the mechanical properties and thermal compatibility of the anode-electrolyte interface require further investigation.

This study aims to understand how the addition of molybdenum oxide (MoOx) to the NiO anode in larger solid oxide fuel cells (9.62 cm^2) affects their performance. The objective is to examine how this alters polarization resistance, current, and power output, using hydrogen and ethanol as fuels.

The changes in structure and microstructure caused by the addition of MoOx will also be investigated using techniques such as XRD, TEM and Raman spectroscopy, aiming to verify how the phases are distributed and how the layers adhere to each other.

Table 1. Overview of literature on direct fuel reforming in SOFCs

Fuel	Catalyst	Power Density (mW cm^{-2})	R_p (ohm.cm^{-2})	Operating Temperature (°C)	Reference
Catalysts for the Direct Reform of Methane/Natural Gas					
Hydrogen	Ni-Fe	>1000	~0.13	750	25
Methane		>1000			
Dry Natural Gas	Ru	410	–	500	26
Methane		440			
Humidified Natural Gas		800		530	
Methane	(SDC)/(Ni-YSZ)	650	~0.20	800	27
Methane	Mo-PBMO	600	~0.11	850	28
Methane	PBMO	~490	~0.14		
Catalysts for Internal Methanol Reform					
Methanol	SBMO	415	–	850	29
Hydrogen	SBMO	480	–	850	
Hydrogen	(SDC)	325	–	750	30
Methanol		350	0. 05		
Catalysts for the Internal Reform of Ethanol in SOFC					
Ethanol	(Ir/CGO)	420	–	850	14
Hydrogen	(Ni/GDC)	58	–	850	15
Ethanol		40	–		
Ethanol	Ni/CeY Ni/CePr Ni/CeZr	Long-term tests (50 h)		850	16
Hydrogen	NiCu/ CGO	370	~0.45	800	11
Hydrogen	NiCo/CGO	500	~0.15		
Ethanol	NiCu/ CGO	275	~0.70		
Ethanol	NiCo/CGO	210	~0.55		
(Hydrogen 97% - H_2O 3%)	Ni-GDC	1660	~0.03	700	17
(Ethanol 70% - N_2 30%)	Ni-GDC	1370	0.04	700	
(Hydrogen 97% - H_2O 3%)	$Sr(Ti_{0.3}Fe_{0.7}Ru_{0.07})O_{3-\delta}$	400	0.26	800	18
Ethanol/H_2O 1:3 - N_2 22%)	$Sr(Ti_{0.3}Fe_{0.7}Ru_{0.07})O_{3-\delta}$	195	0.48	800	
Ethanol 6.5%	Ru-GDC	944.5	0.16	800	21
(H_2O 2.5% + Ethanol 1%) v/v	$Ce_{0.2}Sr_{0.8}Fe_{0.95}Ni_{0.05}O_3$	580	0.13	800	20
Hydrogen	LSCFN-GDC	2110	0.23	800	21
Ethanol	LSCFN-GDC	970	0.54	800	
Hydrogen	Ni-YSZ	2160	~0.21	800	
Ethanol	Ni-YSZ	1360	0.27	800	
Hydrogen	$Ni_{0.9}Cu_{0.1}TiO_{3-\delta}$	1100	0.15	800	22
Ethanol	$Ni_{0.9}Cu_{0.1}TiO_{3-\delta}$	867	0.79	800	
Hydrogen (with 3% of Water)	$Rh/CeZrO_2$	340	–	600	23
35 vol% Ethanol Solution	$Rh/CeZrO_2$	260	–	600	
Catalysts for Direct Gasoline Reform in SOFC					
Gasoline	MoO_2	31	–	750	31
Isooctane/Air	NiMo-Ce-Zr	405	1.36	750	32
Hydrogen		479	0.47		
Isooctane/Air	NiMo-Ce-Zr	392	1.77		
Hydrogen		606	0.42		
Catalyst for Direct Reform of Biodiesel in SOFC					
n-Dodecane	MoO_2	34	-	850	33
Biodiesel		45	-		
Catalysts for Internal Reform of Butane in SOFC					
η-C_4H_{10}	Cu-Co	275	0.30	800	11
Hydrogen	Cu-Co	400	0.15		

This research aims to analyse the electrochemical performance of cells using ethanol directly and link the benefits to the catalytic action of molybdenum oxides. Internal reform processes and how they influence the overall efficiency of the cell will be discussed.

Finally, the possibility of using ethanol and water blends directly as fuel will be discussed, highlighting the potential of the NiO/MoO_x anode for energy production systems that can be scaled up and are sustainable.

Since molybdenum can exist in multiple oxidation states, such as MoO_3, MoO_2 and metallic molybdenum, we opted to use the general term "MoOx" throughout the manuscript to refer to molybdenum oxides, with MoO_2 being the most likely species under the experimental conditions. However, during SOFC operation under reducing conditions (with H_2 or ethanol), molybdenum oxide is expected to be reduced to metallic molybdenum. It is important to note that material characterization was performed after the cell was cooled in an air atmosphere. This cooling process leads to the reoxidation of the metallic molybdenum formed during operation, resulting in the post-operation detection of molybdenum oxide (predominantly) as well as some residual metallic molybdenum.

2. Experimental

2.1. Production of the anode support

The anode was prepared from nickel oxide powders (NiO Fiaxell SOFC Technologies, BET specific surface area of 7.23 m^2/g) and yttria stabilized zirconia (YSZ, 8YSZ Melox, Fiaxell SOFC Technologies, BET specific surface area of 8.3 m^2/g). Dibutylphthalate (DBF, Synth) and polyethylene glycol (PEG, EMFAL) were used as plasticizers, ethanol and toluene as solvents, triton X as dispersant, polyvinyl butyral as binder (PVB, Aldrich Chemistry), and carbon black as pore former. The procedure used to produce the anode support was described in the work of Lee *et al.*[34] The suspension was prepared in two steps, as outlined in Table 2.

Initially, the NiO, YSZ and carbon black powders were mixed with the solvents and dispersants and homogenized in a roller mill for 24 h. Polyvinyl butyral (PVB), dibutyl phthalate (DBP), and polyethylene glycol (PEG) were then added to the vial containing the first-stage mixture and homogenized for an additional 24 hours. After this step, vacuum deaeration was performed for 30 minutes to remove the air in the suspension, and then the tape was obtained using the tape casting technique. After the drying step, circular molds with a diameter of 73 mm were cut and calcined at 1200 °C for 12.5 h, with a heating rate of 1.5 °C min^{-1}. Then, they were sintered at 1300 °C for 7 h, with a heating rate of 3.0 °C min^{-1}, thus obtaining the anode.

2.2. Electrolyte and anode suspensions

The CGO powder containing ZnO at a molar ratio of 49:1 (BET surface area 0.728 m^2/g) was prepared according to the route described in previous work by our group.[35]

The CGO and 1 wt% ZnO powder (Synth) electrolyte suspension were prepared in two steps. In the first step, ethylcellulose, alpha-terpenol and isopropanol were mixed and homogenized for 20 min in a ball mill. In the second step, CGO and 1 wt% ZnO powder (Synth) were added and homogenized for 4 h in the ball mill. Basically, zinc oxide (ZnO) acts as a sintering agent, that is, it reduces the temperature necessary for the CGO particles to join and form a dense and solid part.

The YSZ and NiO suspension materials with and without catalysts are presented in Table 3, All those suspensions were prepared as described for CGO/ZnO.

The surface areas of each powder are presented below: YSZ powder (8YSZ Melox, Fiaxell SOFC Technologies, BET surface area of 8.3 m^2/g); NiO powder (Fiaxell SOFC Technologies, BET surface area between 8-12 m^2 and the NiO and 2.5 wt% powder MoO_x. The precursor of molybdenum oxide used was ammonium molybdate (Synth) PA.

Table 2. Composition of support anode suspension

	Step 1					Step 2			
	Pore Former			Solvent		Dispersant	Binder		Plasticizer
Material	NiO	YSZ	Carbon Black	Ethanol	Toluene	Triton X	PVB	PEG	Dibutyl Phthalate
Weight(g)	42	25	6.7	21	33	2	8.8	2	6.9

Table 3. Compositions of the electrolyte e suspension and catalytic anode

	Material	NiO/MoOx	Nio	YSZ	CGO/Zn	Ethylcellulose	Isopropanol	Alfaterpenol
Weight (g)	Catalytic Anode	8.5	-	-	-	1.05	5.25	19.25
	Anode	-	8.5	-	-	1.05	5.25	19.25
	Electrolyte (YSZ)	-	-	8.5	-	1.05	5.25	19.25
	Electrolyte (CGO/Zn)	-	-	-	8.5	1.05	5.25	19.25

2.3. Cell assembly

Two fuel cells with different anodes were produced: one with NiO and the other with Ni/MoO_2. The elaboration of the cells was carried out from the deposition of several layers as described below. The layers of YSZ, CGO, and NiO were deposited using a brush ((#4, Tiger). The LSCF layers were deposited using the screenprint technique.

11 layers of YSZ were deposited on the anode support, then the electrolyte was calcined and after cooling, sintered. On the YSZ, 4 layers of CGO/ZnO suspension containing 1 wt% ZnO were deposited, and the material was calcined. Since the contact between LSCF and YSZ leads to the formation of an insulating phase of strontium zirconate ($SrZrO_3$),[36] a layer of CGO/ZnO was introduced that acts as a barrier preventing the reaction between the LSCF cathode and the YSZ electrolyte.

Then, on the other anode support side, 11 layers of NiO suspension were deposited in cell (I) and 11 layers of NiO/MoO_x suspension in cell (II) with 2.5 wt% MoO_x, which were calcined. After cooling, the anode was sintered. The calcination steps were carried out up to 1200 °C with a heating rate of 1.5 °C min^{-1}. The electrolytes and catalytic anode were sintered simultaneously at 1350 °C, with a heating rate of 3.0 °C min^{-1}. During sintering, a weight of 3 g/cm^2 was used to avoid cell deformation. 4 layers of commercial LSCF cathode (Fiaxell) were deposited on the CGO. The cathode was sintered at 1030 °C for 2 h. The final complete cell has an anode with a diameter of 50 mm and a cathode with a diameter of 35 mm. To ensure the tightness of the cell during operation, alumina foams were used.

2.4. Characterisation of the cells

XRD analysis was performed using a Diffractometer (Malvern PANalytical Empyrean model) with a Cu tube (Kα = 1.5406 Å), 30.0 kV, and 30.0 mA. Divergence and scatter slit of 1.000 degrees and receiving slit of 0.15000 mm. Scanning procedure in a Theta-2Theta configuration, with a step size of 0.02°, a collection time of 2 seconds, and a 2θ range of 10.00° to 90.00°. Following the ethanol reforming test, the Rietveld refinement of the NiO/MoO_x material and the anode was performed using the Sindarin-Nimloth software (https://nimloth.app). The Rietveld refinement used the NiO, Ni, and YSZ (Y-ZrO_2) standard crystallographic information files (CIF) with the following information: cubic lattice (Fm-3m), space group 225, and ICSD entry #112324, # 238375 and # 53807 for the NiO, YSZ, and Ni materials, respectively. The refinement procedure used a Pseudo-Voigt (convolution of Lorentzian and Gaussian) function profile with a Chebyshev background employing 8 terms. The refinement provided information regarding lattice parameters and phase fractions.

Scanning electron microscopy (SEM) coupled with energy-dispersive spectroscopy (EDS) detector analysis was performed using a Quanta 200/FEG/FEI, with acceleration voltages ranging from 30 kV to 200 kV. The resolution was 1.6 nm at 30 kV in high vacuum and 3.5 nm at 3 kV in low vacuum. High-resolution transmission electron microscopy analysis was performed using a G2-20 TECNAI FEI and the images were analyzed using the Gatan DigitalMicrograph© software. Raman spectroscopy was performed on a Witec alpha 300 RA micro-Raman equipment.

2.5. Electrochemical characterization of the cells produced

Electrochemical measurements were performed using ethanol and hydrogen as fuels. Cell performance was determined using electrochemical impedance spectroscopy (EIS) techniques to determine polarization resistances and galvanostatic voltammetry to determine cell power densities. Electrochemical measurements were performed using a PGSTAT AUTOLAB 30 potentiostat with an FRA impedance module and FRA and GPES software. Electrochemical impedance spectroscopy measurements were performed in the frequency range of 10^4 to 10^{-1} Hz with 10 mV potential perturbation. Electrochemical tests were performed in two-atmosphere furnaces (KITTEC SQUADRO model SQ 11). The parameters used in the electrochemical measurements were based on previous studies and further optimized specifically for this study to ensure accurate and relevant results.

3. Results and Discussion

3.1. Images of cells after the assembly step

The images in Figure 1 reveal that after the sintering stage, the electrolyte and electrode layers deposited on the anode support are regular, consistent and do not present any flaws in their structure. This is a factor that contributes to the good performance of the cells in electrical measurements.

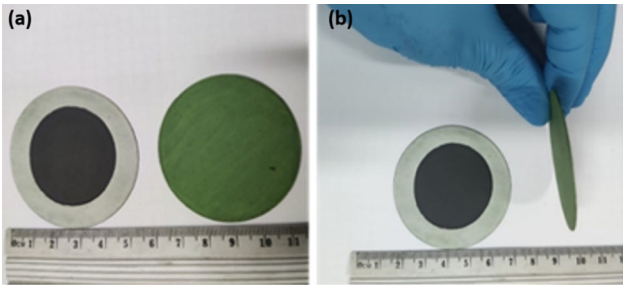

Figure 1. Images of the cells after sintering: (a) cathode and anode NiO/MoO_x and (b) profile and surface

3.2. Morphological and structural characterization

The diffractograms of the NiO/MoO_x and the anode, along with the corresponding standards, are shown in Figure 2(a). The NiO/MoO_x pressed material showed only the cubic

phase (#225) of NiO, with no presence of molybdenum in the diffractogram. Additionally, there is no peak shift or enlargement due to the Mo insertion, leading to the conclusion that Mo is not inserted in the NiO lattice, but due to the low fraction of Mo, it was impossible to characterize its presence. The anode showed the presence of three crystalline phases, including NiO, Ni, and Y-ZrO_2 (YSZ), and all the phases present cubic lattice (#225). Figures 2(b) and (c) show the Rietveld refinement graphs obtained for the NiO/MoO_x and Anode, respectively. All the Rietveld refinement graphs showed good coherence between the experimental and calculated diffractograms, leading to an almost flat difference line, which is crucial to obtaining reliable refinement.[37] Both analyses presented good values for the statistical data, where the NiO and anode showed $\chi^2 = 1.479$ and 2.603, respectively. The NiO presented lattice parameters a = 4.17650(5) Å, a value very close to the standard data (a = 4.1718(1)), thus confirming no major changes in the lattice, evidencing once more that Mo is not inserted in the crystal structure. The Anode refinement aimed to quantify the phase fraction present in the sample, where the NiO, Ni, and YSZ presented a fraction of 52, 44, and 4%, respectively.

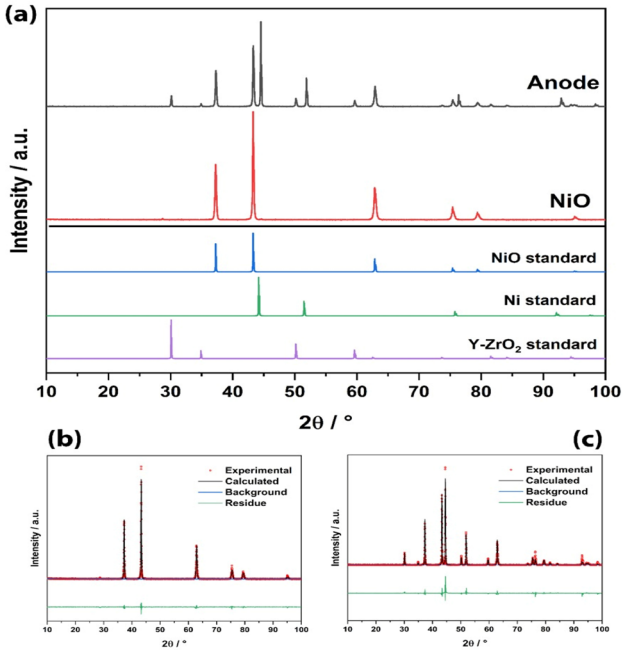

Figure 2. (a) XRD diffractograms of the synthesized NiO powder and the assembled anode, with standard diffractograms used as reference (b) Rietveld refinement graphs for the NiO and (c) anode samples

Figure 3(a) shows a TEM image of the active catalytic layer that contains NiO with molybdenum oxide. The material is micrometer-sized, with different contrasts, evidencing changes in the particle thickness. The circled region labelled "EDS" showed a very high content of Mo, as shown in Figure 3(b).

Although XRD analysis did not detect molybdenum, transmission microscopy could show its presence in the sample.

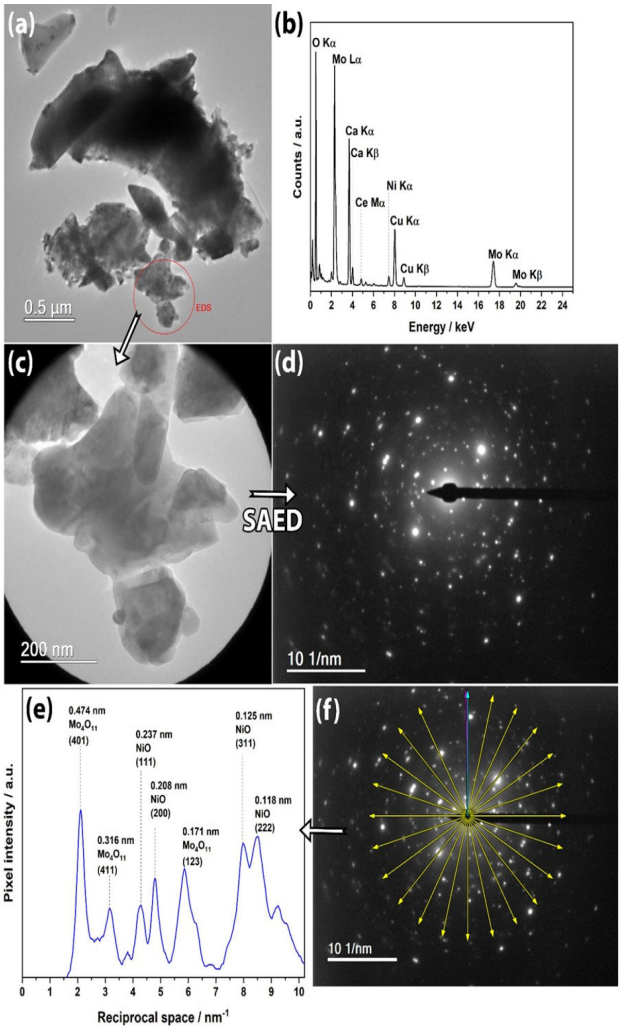

Figure 3. (a) TEM image of the studied material, along with the (b) EDS spectrum of the selected area in Figure 2 (a), (c) higher magnification of the selected area and its respective (d) SAED analysis, (e) showing the reciprocal space values for the d-spacing using the (f) rotational average calculations

Figure 3(c) shows a higher magnification of the EDS region of Figure 3(a), evidencing the presence of some nanoparticles and the coalescence between the material. The selected area electron diffraction (SAED) was carried out in the region shown in Figure 3(c) region to further investigate its structure, evidencing a polycrystalline sample without any preferential orientation. The SAED in Figure 3(d) shows many diffracted spots, leading to difficulty in understanding the sample's crystalline behavior. However, the integer of the pixels using the rotational average operation clarified the diffracted spots, where the reciprocal space x pixel intensity curve in Figure 3(e) of the rotational average (Figure 3(f)) showed high intensity for the plane with d-spacing of 0.474 nm, which corresponds to the (401) plane of Mo_4O_{11} oxide,[38] with other planes also corresponding to the Mo_4O_{11} phase, such as (411) and (123). The remaining crystal planes correspond to the NiO oxide, such as the (111), (200), (222), and (311).

A higher magnification of the region rich in molybdenum

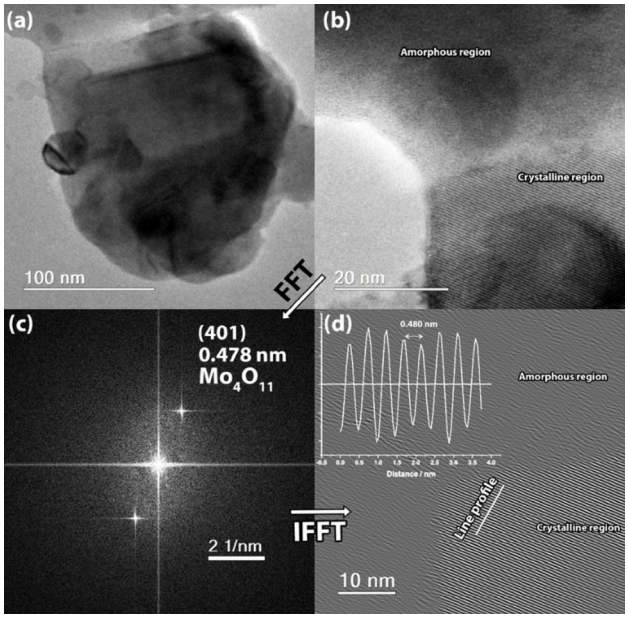

Figure 4. (a) TEM image of the region shown in Figure 3, with (b) higher magnification HRTEM image showing its crystalline behaviour (c) FFT of Figure 3 (b) presenting the correspondent Bragg spots and their (d) IFFT evidencing the crystalline region with a d-spacing of 0.480 nm

is shown in Figure 4(a). The HRTEM image (Figure 4(b)) shows the coalescence between particles, evidencing an amorphous and crystalline region. The fast Fourier transform (FFT) in Figure 4(c) shows two Bragg spots that correspond to a d-spacing of 0.48 nm, evidencing the (401) plane of Mo_4O_{11}. The crystalline region is evidenced after filtering the Bragg spots and applying an inverse fast Fourier transform (IFFT). The line profile in Figure 4(d) shows a d-spacing measurement directly from the crystalline region of the image, once more showing a d-spacing of 0.48 nm. Despite the small quantity of evidence of molybdenum presence employing XRD, the EDS and HRTEM analysis led to the conclusion that the molybdenum in the sample is in the form of an oxide rich in oxygen, which improved the physical contact between the active catalytic layer and the anode substrate, as shown in the scanning electron microscopy (SEM) analysis.

The Raman spectrum of an anode fragment (Figure 5) confirms the presence of molybdenum oxides (MoO_2 and/or MoO_3) represented by peaks located approximately at 990, 820, 670, 340, 286 e 156 cm^{-1}. It is not easy to separate the peaks corresponding to each oxide. The other peaks (red arrows) are characteristic of NiO.[39]

Figure 6(a) shows the complete cell with all constituent layers successfully deposited. Figure 6(b) shows the interface between the supporting anode and the catalytic layer without Mo oxide. The NiO layer is not regular and its adhesion to the support is not satisfactory, resulting in the detachment and the appearance of flaws in the layer. Figure 6(c) shows the micrograph of the interface anode support / catalytic anode of the cell containing Mo oxide, clearly showing that this introduction favored the adhesion

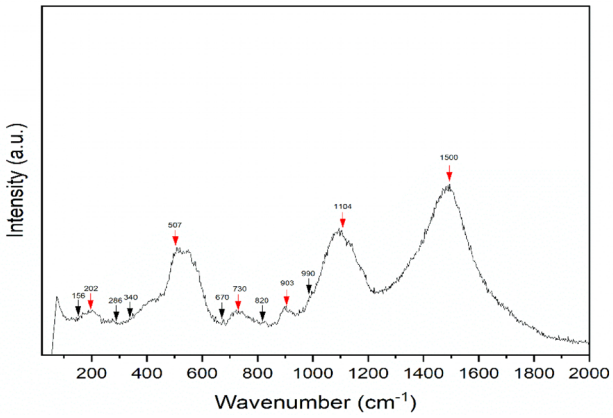

Figure 5. Raman spectrum of the anode

ofthe layer, which appeared without cracks and layer detachments. The deposited layer is also regular, having the same thickness throughout.

3.3. Electrochemical impedance measurements

The heating ramp and gas flows used before the electrochemical tests performed are indicated in Table 4.

The second heating stage involves introducing a stream of hydrogen (H_2) to the cell anode, starting with a low flow of 20 mL min^{-1}, gradually increasing every 20 up to 200 mL min^{-1} to promote anode reduction. The ethanol-water mixture was introduced into the cell during electrical measurements using a peristaltic pump (Lead Fluid: BT101L). Table 5 outlines the fuel flows utilized in the cell test using H_2 and 1:3 ethanol-water mixture. Experiments 1 and 2 correspond to the different fuels and flow rates used in both cells, with and without the catalyst.

Figure 7 shows the impedance plots, in the Nyquist plane, for the NiO anode and NiO/Mo_x anode cells, fed with hydrogen fuels as standard and ethanol for the reform tests.

In this study, the inductance effects from the instrument and connecting wires were eliminated. In the EIS Nyquist plot for the SOFC, the high-frequency intercept typically corresponds to the ohmic resistance of the electrolyte. Figure 8 illustrates the equivalent circuit model, featuring a series resistance element connected with two parallel R–CPE elements. R_1 (intersection of the semic**ir**cle with the real axis) represents high -frequency resistance, usually attributed to the ohmic resistance of the cell: electrolyte, interfaces and electrical contacts. While R_2 and R_3 correspond to the Middle- and low-frequency process resistances, with CPE_1 and CPE_2 as their respective constant-phase elements. The sum of these two resistances corresponds to the polarization resistance, R_p reflects the losses associated with the kinetics of electrochemical reactions and the processes of mass (gas) and charge (electrons and ions) transport in the electrodes.

The impedance results (Table 6) showed that in measurements using hydrogen (Experiment I) and ethanol (Experiment II) as fuel, the cell containing the NiO anode

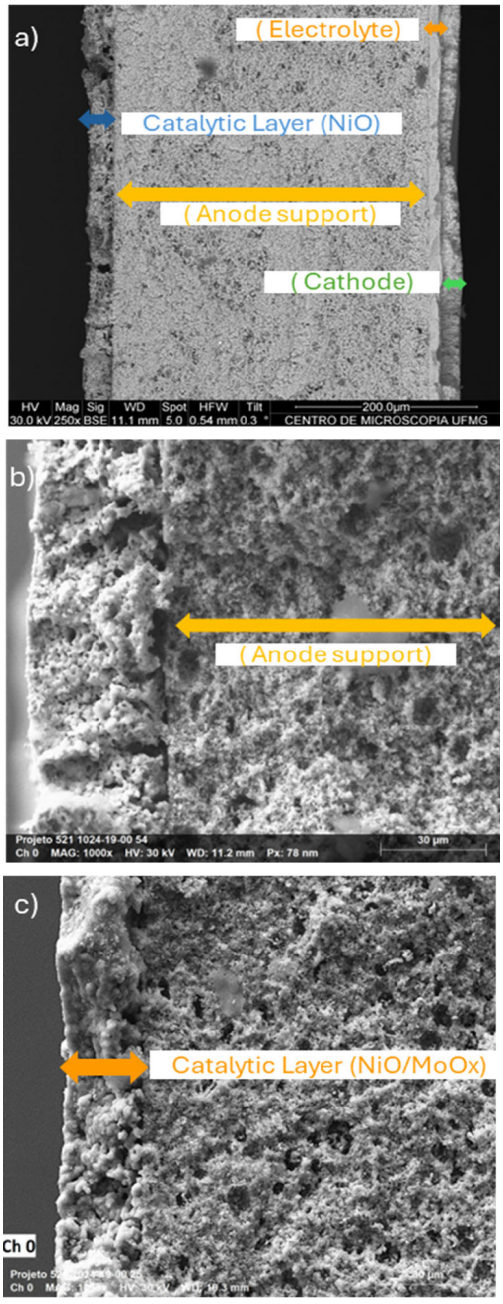

Figure 6. Scanning electron microscopy of cell layers (a) complete cell without MoO_x (b) interface between the supporting anode and the catalytic layer, without the presence of MoO_x, and (c) interface between the supporting anode and the catalytic layer, with the presence of MoO_x

showed higher R_1 e R_p than the cell containing the NiO/MoO_x anode.

The decrease in ohmic resistance can be explained by the properties of molybdenum in improving the physical and chemical contact between the support anode and the catalytic anode, increasing the electronic conductivity.[33,40] Among metals, molybdenum stands out for its low coefficient of thermal expansion.[40] Studies indicate that adding molybdenum to nickel-based alloys significantly reduces the thermal expansion coefficient of the solid solution.[24] Incorporating of molybdenum into NiO anodes can reduce the coefficient of thermal expansion from 15×10^{-6} K^{-1} [41] to a value compatible with Ni/YSZ (12.37×10^{-6} K^{-1}).[42] This thermal compatibility is crucial for preventing stress during heating and cooling cycles, reducing the risk of delamination or interfacial fracture between the catalytic NiO/MoO_x anode and the Ni/YSZ anode support.

Molybdenum can form surface oxides (such as MoO_x) that can chemically interact with the YSZ surface, creating a chemically adherent interface. This reactivity can promote stronger bonding between catalytic anode and anode support, improving adhesion.[43] Additionally, molybdenum can alter the microstructure of the anode layer, increasing the effective contact area with the support anode. A rougher or more porous interface can provide superior mechanical adhesion due to greater interlocking of the layers at the interface. Molybdenum can also enhance the mechanical properties of the anode layer, increasing its fracture resistance and its ability to accommodate deformations without detaching from the anode support.[44]

The decrease in polarization resistance can be explained by several factors interconnected with the addition of metal oxides: i) increased electrocatalytic activity in relation to hydrogen oxidation and ethanol reforming. The manuscript highlights the presence of multiple oxidation states for molybdenum specifically MoO_2, MoO_3, and Mo_4O_{11}, which play distinct roles in the catalyst's performance. MoO_2 is known for its conductive properties, which can enhance electron transfer, while MoO_3 and Mo_4O_{11} are more active in oxygen transfer and redox reactions. The combination of these oxidation states likely contributes to both efficient ethanol reforming and improved overall catalytic performance. This reduction of polarization resistance agrees with the formation of multiple Mo oxidative states that increase the oxygen vacancies, improving the electrical conductivity of the Mo oxide electrode.[31]; ii) increase in the surface area of the three-phase region, where the gaseous fuel and the electronic and ionic conductive phases meet, enabling electrochemical reactions to oxidize the fuel. Mesoporous materials, such as those mentioned in the study by Díaz-Aburto *et al.*[45] for Mo-CeO_2/YSZ anodes, are designed to maximize TPB and thus improve

Table 4. Heating conditions and flows prior to electrochemical testing

Step	Temperature °C	Time (h)	Flow (mL min^{-1})		Gas
1ª	25 - 740	2	400	cathode and anode	Ar
2ª	740	0.5	400	cathode	Ar
			20 to 200	anode	H_2

Table 5. Fuel flows utilized in the cell tests

Experiment 1 (mL min^{-1})		Experiment 2 (mL min^{-1})	
H_2	100	C_2H_5OH/H_2O	0.03
O_2	400	O_2	400

electrochemical performance; iii) Improvement of mass transport (diffusion of combustible gas). The presence of molybdenum in the catalytic layer can improve porosity, facilitating the diffusion of fuel to the reaction sites and the removal of products.[46]

3.4. Evaluation of the internal reform from the measures of power densities

In the initial experiment using hydrogen as fuel in NiO and NiO/MoO_x cells, the cell with the Mo catalyst showed superior performance. Subsequently, the performance of the fuel cell with and without the Mo catalyst was compared during ethanol reforming. The best results were obtained with ethanol solution flow rates of 0.03 and 0.06 mL min^{-1}. Using a 1:3 ethanol-water mixture at 0.03 mL min^{-1}, the Mo-catalyzed cell again performed better. When the flow rate was increased to 0.06 mL min^{-1}, the performance of the cell was probably decreased due to excess fuel. Figure 9 shows the maximum power values delivered by cells having NiO and NiO/MoO_x anodes operating with hydrogen and ethanol.

The ethanol solution performed better than hydrogen. This is a surprising result, especially if we calculate the theoretical amount of hydrogen produced in the internal reform.

Steam catalytic reforming stands out among the thermal methods for producing hydrogen from ethanol. This is due to its high hydrogen yield, high reaction rates, and good endothermicity. The main ethanol steam reforming reaction is given by:

$$CH_3CH_2OH + 3H_2O \rightarrow 6H_2 + 2CO_2 \quad \Delta H^0_{298} = 174.2 \text{ kJ/mol} \quad (1)$$

Despite having a main endothermic reaction, ethanol reforming for hydrogen production can generate unwanted byproducts due to secondary ethanol decomposition reactions. Scientific literature points to the formation of various species, such as H_2, CO, CO_2, CH_4, ethylene, ethanol, acetaldehyde, acetone, and coke.[47, 48]

Considering a flow of 0.03 ml of the ethanol/water solution 1/3 at a temperature of 750 °C and at a pressure of 1 atm. The amount of hydrogen theoretically produced completely and optimally by reaction (1) would be approximately 65 mL/min.

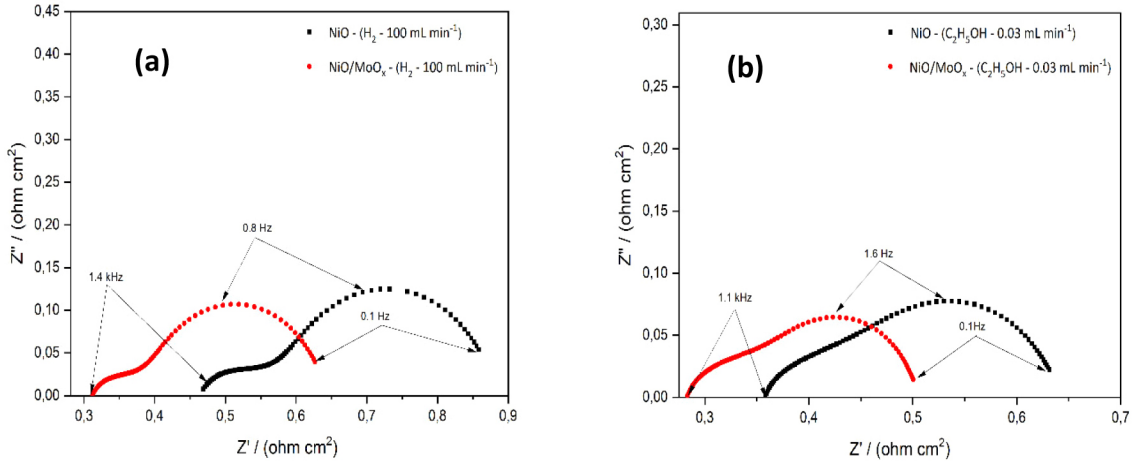

Figure 7. Impedance diagram in the Nyquist plane obtained at 740 °C for cells with NiO and NiO/MoOx anodes: (a) operating with H_2 (b) operating with C_2H_5OH

Table 6. Fitting results of resistances

Experiment	Cell	R_1 (ohm cm^2)	R_P (ohm cm^2)
I	NiO	0.45	0.43
	NiO/MoO_x	0.31	0.33
II	NiO	0.36	0.28
	NiO/MoO_x	0.28	0.23

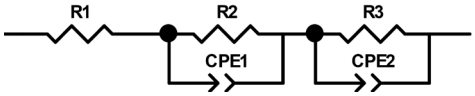

Figure 8. Representation of the proposed equivalent circuit

This unexpected behavior can be explained by a particularly effective internal reform of ethanol. The presence of water in the fuel mixture used is crucial for steam reforming, as it reacts with ethanol to produce H_2 and CO_2 and can also react with CO (gas-water displacement reaction) to produce more H_2. If the catalytic layer is particularly effective in promoting these reforming and displacement reactions, the in-situ production of H_2 and CO can be as efficient, or even more so, than the direct supply of H_2, leading to lower polarization resistance.

Some studies show that certain anode materials may perform better with liquid fuels or hydrocarbons than with pure hydrogen. For example, Boldrin *et al*. (2016)[49] mention that anodes may outperform operating with direct ethanol than hydrogen, correlating this performance increase to an improvement in catalytic activity and resistance to carbon deposition. The internal reform of fuels such as ethanol can be beneficial for the thermal management of the cell. Hariharan *et al*. (2024)[50] discuss the advantages of direct internal refurbishment in SOFCs, such as improved thermal management and faster response time, which can lead to superior overall performance and, consequently, lower resistances.

The measurement results (Figure 9) demonstrate that introducing molybdenum (Mo) into the nickel oxide (NiO) anode promotes a significant increase in the power generated by the fuel cell. When using hydrogen as fuel, the power increased from 345.6 to 378.4 without and with the Mo catalyst, according Figure 9a.

The NiO/MoO_x anode demonstrated superior reforming performance when ethanol was used as fuel, with the Mo-catalyzed cell generating higher power at all tested ethanol flow rates. However, increasing the ethanol flow to 0.06 mL min^{-1} reduced the power output in both cells, highlighting the anode's limitations at higher fuel flow rates. Despite this, the reduction was less significant in the Mo-containing cell, confirming the catalyst's beneficial impact on the NiO anode's reforming capacity. Overall, adding Mo to the NiO anode enhances fuel cell performance with both hydrogen and ethanol.

Many works confirm that functional cathode[42] and/or anode layers[51] in the fuel cell composition enhance both polarization resistance and cell power density. The best result of power density presents in the introduction of this work concerning SOFC fuel catalysts was greater than 1000 mW cm^{-2} with a nickel-iron catalyst for reforming methane at 750 °C, using a cell with an anode layer functional.[25]

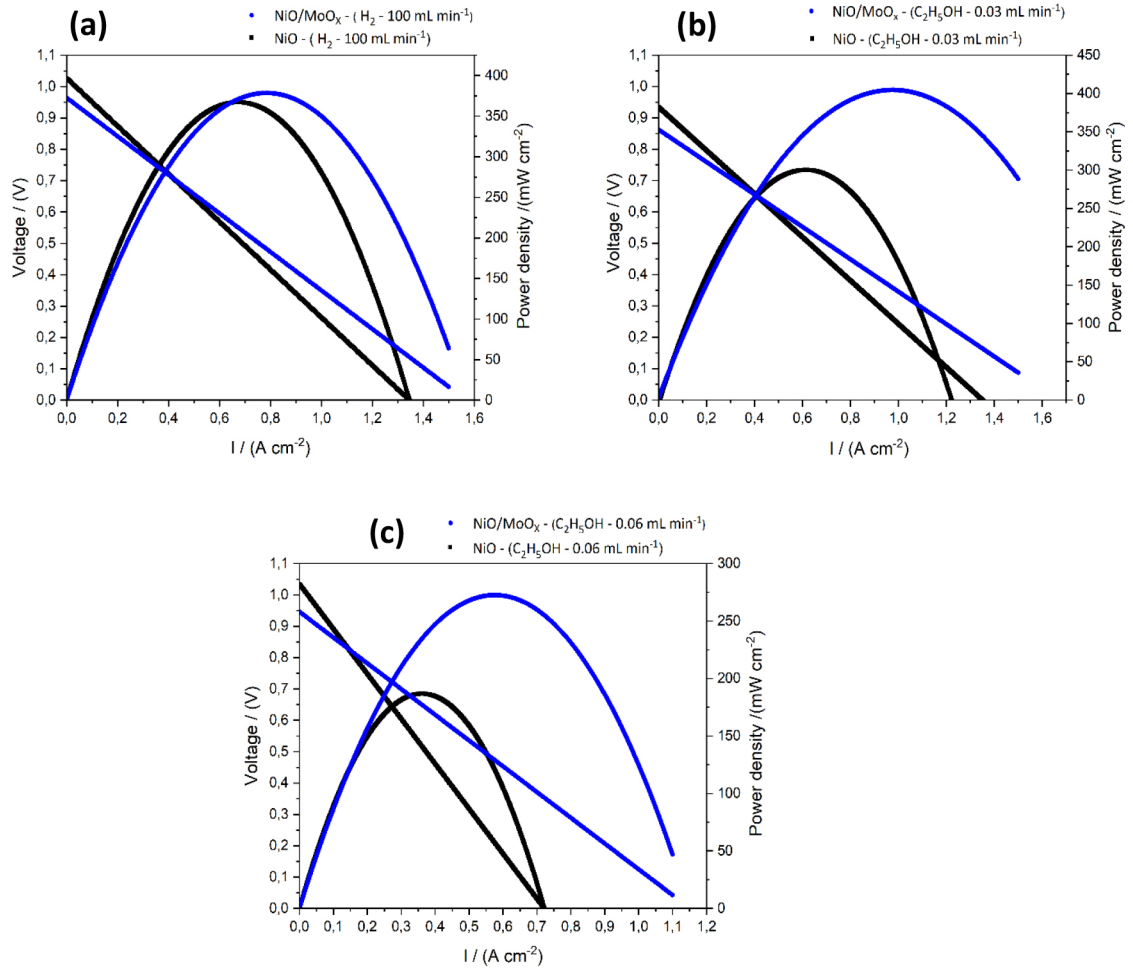

Figure 9. Power density curves at 740 °C. (a) H_2 (100 mL min^{-1}); (b) C_2H_5OH (0.03 mL min^{-1}) and (c) C_2H_5OH (0.6 mL min^{-1})

For the long-chain fuels, the best result was 405 mW cm^{-2}, obtained with the anode of (NiMo-CZ), containing the Mo and Ce as catalysts, besides the nickel, in reforming the gasoline at 750 °C.[32]

In this study, the cell produced with a Mo oxide catalyst and tested with a 1:3 v/v ethanol-water mixture exhibited a polarization resistance (Rp) of 0.23 ohm cm^2 and a power density of 404,4 mW cm^2 at 740 °C. This result is particularly impressive given the absence of a functional layer, representing a 107% increase in power density compared to reference 43 that shows the same fuel mixture. Additionally, the experiments were conducted at a temperature of 60 °C lower than the previous test.

3.5. Relationship between electrochemical properties and material structure

The electrochemical performance of solid oxide fuel cells (SOFCs) is intrinsically linked to the structural properties of the materials used in the anode, electrolyte, and cathode. One of the key factors influencing electrochemical behavior is the microstructure of the materials, including porosity, grain size, phase distribution, and the presence of catalytic phases such as molybdenum oxide (MoO_x).

The addition of MoO_x to the Ni-based anode plays a critical role in enhancing both the electrochemical properties and the mechanical stability of the anode. MoO_x acts not only as a catalyst but also modifies the microstructure of the anode, improving its overall performance. The enhanced catalytic activity observed in this study can be attributed to the formation of fine and uniformly distributed MoO_x particles within the Ni matrix, which promote better fuel reforming, especially in ethanol-based SOFCs. This is critical for reducing polarization resistance, as the improved catalytic sites enhance fuel conversion and reduce the accumulation of intermediates like carbon, which would otherwise hinder the electrochemical reactions.

Furthermore, the porosity and pore distribution in the anode structure affect the gas diffusion, which in turn influences the polarization resistance and power density of the cell. The presence of MoO_x contributes to a more stable porous structure that facilitates the transport of reactants and products within the anode, enhancing the electrochemical reactions at the triple-phase boundary (TPB). A well-structured anode with optimal porosity ensures better connectivity between the Ni particles and the electrolyte, which is critical for ion transport and the overall electrochemical performance.

3.6. Application of the approach to other biofuels

While this study focuses on ethanol as a fuel for SOFCs, the approach of incorporating molybdenum oxide (MoO_x) into the anode material to enhance catalytic performance and thermal compatibility can also be extended to other biofuels such as biodiesel and biogas. Each of these biofuels presents unique challenges in terms of reforming efficiency, carbon deposition, and thermal stability, but similar strategies can be applied to mitigate these issues.

Ethanol is already a widely studied biofuel for SOFCs due to its high hydrogen content and ease of reforming. The addition of MoO_x to the anode has shown promise in reducing carbon buildup and improving fuel conversion efficiency. This approach can be further explored in ethanol-based SOFC systems to enhance power density and operational stability over long periods.

Biodiesel, composed of long-chain fatty acid methyl esters, presents greater challenges in terms of reforming due to its complex molecular structure, which increases the risk of carbon deposition and incomplete fuel utilization. The catalytic properties of MoO_x could assist in breaking down the larger hydrocarbon chains more efficiently, potentially improving the reforming process and reducing carbon formation. Furthermore, the thermal compatibility benefits observed with MoO_x could help in maintaining stable operation at the high temperatures required for biodiesel reforming in SOFCs.

Biogas, which typically consists of methane and carbon dioxide, is another promising biofuel for SOFC applications. The direct internal reforming of biogas in SOFCs can lead to issues such as carbon formation due to methane cracking. The incorporation of MoO_x into the anode could enhance the catalytic activity for methane reforming, reducing carbon buildup and improving the overall performance of the SOFC. Additionally, the enhanced thermal compatibility provided by MoO_x can mitigate thermal stresses caused by the fluctuating composition and quality of biogas.

In summary, the strategy of incorporating MoO_x into SOFC anodes can be effectively applied to a range of biofuels, including ethanol, biodiesel, and biogas, to improve system performance and thermal compatibility. This approach opens the door to the broader use of renewable fuels in SOFC systems, contributing to more sustainable energy production across various applications.

4. Conclusion

This study complements the existing literature by contributing to the understanding of molybdenum as a catalyst for fuel reforming reactions in SOFCs, particularly in cells with a large active area. Unlike the more commonly studied button cells, this work focuses on larger active area cells, demonstrating the effectiveness of molybdenum in this less explored configuration. This advancement provides valuable insights into scaling up SOFC technologies while maintaining efficient fuel reforming capabilities.

The incorporation of molybdenum oxide (MoO_x) into the Ni-based anode of SOFCs enhanced catalytic activity and improved thermal compatibility, particularly in cells operating with ethanol as fuel. The main research hypothesis, which postulated that the MoO_x-modified anode

would lead to improved performance through enhanced catalytic activity and thermal stability, was validated by the results. Specifically, the polarization resistance was significantly reduced and the power density increased, especially under ethanol reforming conditions.

The novelty of this work lies in the application of MoO_x as a dual-functional additive, improving both the electrochemical performance and the structural integrity of the anode. This advancement addresses critical challenges in SOFC technology, particularly for the use of biofuels, by providing a pathway to optimize the anode-electrolyte interface and mitigate issues related to carbon deposition.

In summary, this research contributes to the development of more efficient and durable SOFC systems, offering valuable insights for scaling up fuel cell technologies while maintaining high performance. Future work could explore the long-term stability of the catalyst and its application to other renewable fuels, further expanding the potential applications of this approach.

Declaration of Competing Interest

The authors declare that they have no known competing financial interests or conflicts of interest that could have appeared to influence the work reported in this paper.

Acknowledgment

This work was supported by Fundação de Amparo à Pesquisa de Minas Gerais (FAPEMIG), Conselho Nacional de Pesquisa (CNPq, process 405837/2022-4) and Coordenação de Aperfeiçoamento de Pessoal de Nível Superior (CAPES). This work was carried out using the facilities of the Laboratory of Characterization and Processing of Nanomaterials (LCPNano) and Centre of Microscopy of UFMG.

Bibliographic References

1. Shaheen, K.; Shah, Z.; Gulab, H.; Hanif, M. B.; Faisal, S.; Suo, H.; Metal oxide nanocomposites as anode and cathode for low temperature solid oxide fuel cell. *Solid State Sciences* **2020**, *102*, 106162. [Crossref]
2. Department of Economic and Social Affairs Sustainable Development. Disponível em: <https://sdgs.un.org/goals. >. Acesso em: 07 junho 2025.
3. Martins, R. F.; Brant, M. C.; Domingues, R. Z.; Paniago, R. M.; Sapag, K.; Matencio, T.; Synthesis and characterization of NiO-YSZ for SOFCs. *Materials Research Bulletin* **2009**, *44*, 451. [Crossref]
4. Fernandes, M. D.; Bistritzki, V.; Domingues, R. Z.; Matencio, T.; Rapini, M.; Sinisterra, R. D.; Solid oxide fuel cell technology paths: National innovation system contributions from Japan and the United States. *Renewable and Sustainable Energy Reviews* **2020**, *127*, 109879. [Crossref]
5. Hanif, M. B.; Gao, J. T.; Shaheen, K.; Wang, Y. P.; Yasir, M.; Zhang, S. L.; Li, C. J.; Li, C. X.; Performance evaluation of highly active and novel $La_{0.7}Sr_{0.3}Ti_{0.1}Fe_{0.6}Ni_{0.3}O_{3-\delta}$ material both as cathode and anode for intermediate-temperature symmetrical solid oxide fuel cell. *Journal of Power Sources* **2020**, *472*, 228498. [Crossref]
6. Shaheen, K.; Shah, Z.; Ahmed, A.; Structural and electrochemical evaluation of symmetrical and fuel flexible perovskite electrode for low temperature solid oxide fuel cell. *International Journal of Hydrogen Energy* **2024**, *72*, 1069. [Crossref]
7. Akhairi, M. A. F.; Kamarudin, S. K.; Catalysts in direct ethanol fuel cell (DEFC): An overview. *International Journal of Hydrogen Energy* **2016**, *41*, 4214. [Crossref]
8. Hotza, D.; Diniz da Costa, J. C.; Fuel cells development and hydrogen production from renewable resources in Brazil. *International Journal of Hydrogen Energy* **2008**, *33*, 4915. [Crossref]
9. https://ethanolrfa.org/resources/industry/statistics/. Disponível em: < https://ethanolrfa.org/resources/industry/statisti>. Acesso em: 07 junho 2025.
10. Drasbæk, D. B.; Welander, M. M.; Traulsen, M. L.; Sudireddy, B. R.; Holtappels, P.; Walker, R. A.; Operando characterization of metallic and bimetallic electrocatalysts for SOFC fuel electrodes operating under internal methane reforming conditions. *Journal of Materials Chemistry A* **2022**, *10*, 5550. [Crossref]
11. Lo Faro, M.; Reis, R. M.; Saglietti, G. G. A.; Zignani, S. C.; Trocino, S.; Frontera, P.; Antonucci, P. L.; Ticianelli, E. A.; Aricò, A. S.; Investigation of Ni-based alloy/CGO electro-catalysts as protective layer for a solid oxide fuel cell anode fed with ethanol. *Journal of Applied Electrochemistry* **2015**, *45*, 647. [Crossref]
12. Bkour, Q.; Zhao, K.; Scudiero, L.; Han, D. J.; Yoon, C. W.; Marin-Flores, O. G.; Norton, M. G.; Ha, S.; Synthesis and performance of ceria-zirconia supported Ni-Mo nanoparticles for partial oxidation of isooctane. *Applied Catalysis B: Environmental* **2017**, *212*, 97. [Crossref]
13. Bkour, Q.; Che, F.; Lee, K. M.; Zhou, C.; Akter, N.; Boscoboinik, J. A.; Zhao, K.; Gray, J.; Saunders, S. R.; Grant Norton, M.; McEwen, J. S.; Kim, T.; Ha, S.; Enhancing the partial oxidation of gasoline with Mo-doped Ni catalysts for SOFC applications: An integrated experimental and DFT study. *Applied Catalysis B: Environmental* **2020**, *266*, 118626. [Crossref]
14. Steil, M. C.; Nobrega, S. D.; Georges, S.; Gelin, P.; Uhlenbruck, S.; Fonseca, F. C. Durable direct ethanol anode-supported solid oxide fuel cell. *Applied Energy* **2017**, *199*, 180. [Crossref]
15. Noronha, B.; Fonseca, F. C.; Nickel / gadolinium-doped ceria anode for direct ethanol solid oxide fuel cell. *International Journal of Hydrogen Energy* **2014**, *38*, 11196. [Crossref]
16. Silva, A. A. A.; Bion, N.; Epron, F.; Baraka, S.; Fonseca, F. C.; Rabelo-neto, R. C.; Mattos, L. V; Noronha, F. B.; Applied Catalysis B : Environmental Effect of the type of ceria dopant on the performance of Ni / CeO_2 SOFC anode for ethanol internal reforming. *Applied Catalysis B: Environmental* **2017**, *206*, 626. [Crossref]

17. Zhang, L.; Huan, D.; Zhu, Z.; Liu, F.; Dong, D.; Xia, C.; A coking-tolerance dendritic anode with exceptional power density toward direct ethanol-fueled solid oxide fuel cells. *Materials Today Energy* **2023**, *34*, 101290. [Crossref]
18. Donazzi, A.; Schmauss, T. A.; Barnett, S. A.; Catalytic and electrocatalytic performance of $Sr(Ti_{0.3}Fe_{0.7}Ru_{0.07})O_{3-\delta}$ for applications in solid oxide fuel cells supplied with ethanol steam reforming mixtures. *Journal of Power Sources* **2022**, *551*, 232215. [Crossref]
19. Liu, F.; Gao, Y.; Li, J.; Wei, T.; Ye, Z.; Zhang, T.; Dong, D.; Wang, Z.; Direct ethanol solid oxide fuel cells integrated with internal reforming for renewable power generation. *Separation and Purification Technology* **2022**, *298*, 121678. [Crossref]
20. Li, B.; Irvine, J. T. S.; Ni, J.; Ni, C.; High-performance and durable alcohol-fueled symmetrical solid oxide fuel cell based on ferrite perovskite electrode. *Applied Energy* **2022**, *306*, 118117. [Crossref]
21. Zhang, P.; Lei, Z.; Zhang, X.; Yang, Z.; Ling, Y.; Peng, S.; High-stable power generation from low concentration ethanol by catalyst layer modified solid oxide fuel cells. *Journal of Alloys and Compounds* **2022**, *916*, 165448. [Crossref]
22. Rao, M.; Chen, Z.; Deng, Q.; Li, M.; Zhang, Z.; Li, S.; Xiong, K.; Chen, C.; Xue, Y.; Qi, M.; Ou, X.; Tian, Y.; Ling, Y.; Investigation the $Ni_{0.9}Cu_{0.1}TiO_{3-\delta}$ reforming layer for direct ethanol solid oxide fuel cells. *International Journal of Hydrogen Energy* **2023**, *48*, 18871. [Crossref]
23. Elharati, M. A.; Dewa, M.; Bkour, Q.; Mohammed Hussain, A.; Miura, Y.; Dong, S.; Fukuyama, Y.; Dale, N.; Marin-Flores, O. G.; Ha, S.; Internal Reforming Solid Oxide Fuel Cell System Operating under Direct Ethanol Feed Condition. *Energy Technology* **2020**, *8*. [Crossref]
24. Iii, H. M.; Sponseller, D. L.; Semchyshen, M.; The Effects of Molybdenum and Aluminum on the Thermal Expansion Coefficients of Nickel-Base Alloys. *Metallurgical Transactions A* **1975**, *6A*, 477. [Crossref]
25. Park, Y. M.; Kim, H.; An additional layer in an anode support for internal reforming of methane for solid oxide fuel cells. *International Journal of Hydrogen Energy* **2014**, *39*, 16513. [Crossref]
26. Takagi, Y.; Kerman, K.; Ko, C.; Ramanathan, S.; Operational characteristics of thin film solid oxide fuel cells with ruthenium anode in natural gas. *Journal of Power Sources* **2013**, *243*, 1. [Crossref]
27. Chen, Y.; Zhang, Y.; Lin, Y.; Yang, Z.; Su, D.; Han, M.; Chen, F.; Direct-methane solid oxide fuel cells with hierarchically porous Ni-based anode deposited with nanocatalyst layer. *Nano Energy* **2014**, *10*, 1. [Crossref].
28. Sun, Y.; Zhang, Y.; Hua, B.; Behnamian, Y.; Li, J.; Cui, S.; Molybdenum doped $Pr_{0.5}Ba_{0.5}MnO_{3-\delta}$ (Mo-PBMO) double perovskite as a potential solid oxide fuel cell anode material. *Journal of Power Sources* **2016**, *301*, 237. [Crossref]
29. Hou, N.; Li, P.; Lv, T.; Yao, T.; Yao, X.; Gan, T.; Fan, L.; $Sm_{0.5}Ba_{0.5}MnO_{3-\delta}$ anode for solid oxide fuel cells with hydrogen and methanol as fuels. *Catalysis Today* **2017**, *298*, 33. [Crossref]
30. Elleuch, A.; Halouani, K.; Li, Y.; Bio-methanol fueled intermediate temperature solid oxide fuel cell: A future solution as component in auxiliary power unit for eco-transportation. *Materials & Design* **2016**, *97*, 331. [Crossref]
31. Hou, X.; Marin-Flores, O.; Kwon, B. W.; Kim, J.; Norton, M. G.; Ha, S.; Gasoline-fueled solid oxide fuel cell using MoO_2-Based Anode. *Journal of Power Sources* **2014**, *268*, 546. [Crossref]
32. Zhao, K.; Hou, X.; Bkour, Q.; Norton, M. G.; Ha, S.; NiMo-ceria-zirconia catalytic reforming layer for solid oxide fuel cells running on a gasoline surrogate. *Applied Catalysis B: Environmental* **2018**, *224*, 500. [Crossref]
33. Wan, B.; Ellefson, C.; Breit, J.; Kim, J.; Norton, M. G. Molybdenum dioxide-based anode for solid oxide fuel cell applications. *Journal of Power Sources* **2013**, *243*, 203. [Crossref]
34. Lee, S.; Lee, K.; Jang, Y. hoon; Bae, J.; Fabrication of solid oxide fuel cells (SOFCs) by solvent-controlled co-tape casting technique. *International Journal of Hydrogen Energy* **2017**, *42*, 1648. [Crossref]
35. Figueiredo, J. A.; Santos, D.; Horizonte, B.; *Otimização da Microestrutura de Componentes de Pilhas a Combustível de Óxido Sólido a Temperaturas Intermediárias*, Thesis, Universidade Federal De Minas Gerais, 2014. [Link]
36. K. Cheng *et al.*; Numerical Simulation of the $SrZrO_3$ Formation in Solid Oxide Fuel Cells. *Journal of Electronic Materials* **2019**, *48*, 5510. [Crossref]
37. Toby, B. H.; R factors in Rietveld analysis: How good is good enough? **2006** . *Powder Diffraction* **2006**, *21*, 67. [Crossref]
38. Åsbrink, S.; Kihlborg, L.; A Study of the Crystal Symmetry and Structure of Orthorhombic Mo_4O_{11} by Least-squares Techniques. *Acta Chemica Scandinavica* **1964**, *18*, 1571. [Crossref]
39. Ali Moulahi.; Controlled Hydrothermal Synthesis of_Nano-MoO_2 as_Anode_for_Lithium_Ion_Battery. *Indian Journal of Science and Technology* **2020**, *13*, 277. [Crossref]
40. Gritsch, M.; Piplits, K.; Hutter, H.; Wilhartitz, P.; Wildner, H.; Martinz, H. P.; Investigations on the oxidation behavior of technical molybdenum foils by means of secondary-ion mass spectrometry, *Surface Science* **2000**. *454*, 284. [Crossref]
41. Marrero-López, D.; Peña-Martínez, J.; Ruiz-Morales, J. C.; Pérez-Coll, D.; Martín-Sedeño, M. C.; Núñez, P.; Applicability of $La_2Mo_{2-y}W_yO_9$ materials as solid electrolyte for SOFCs. *Solid State Ion*ics **2007**, *178*, 1366. [Crossref]
42. Yousaf, M.; Akbar, M.; Hu, E.; Dong, Y.; Akhtar, M. N.; Yousaf Shah, M. A. K.; Mushtaq, N.; Lu, Y.; Yan, S.; Zhu, B.; Tuning ORR electrocatalytic functionalities in CGFO-GDC composite cathode for low-temperature solid oxide fuel cells. *Ceramics International* **2023**, *49*, 6030. [Crossref]
43. Dhanabalan, K.; Bhosale, M.; Sriram, G.; Sadhasivam, T.; Oh, T. H.; An Investigation of the Interface between Transition Metal Oxides (MnO_x, FeO_x, CoO_x and NiO_x)/MoO_3 Composite Electrocatalysts for Oxygen Evolution Reactions. *Inorganics* **2024**, *12*, 241. [Crossref]
44. Gao, J. T.; Li, J. H.; Wang, Y. P.; Li, C. J.; Li, C. X.; Self-Sealing Metal-Supported SOFC Fabricated by Plasma Spraying and Its Performance under Unbalanced Gas Pressure. *Journal of Thermal Spray Technology* **2020**, *29*, 2001. [Crossref]
45. Díaz-Aburto, I.; Colet-Lagrille, M.; Fuentes, I.; Herrera-Maldonado, M.; Donoso García, P.; Tasca, F.; Zagal, J. H.; Fuel

flexible SOFC with a Mo-doped CeO_2/YSZ mesoporous anode fabricated by the evaporation induced self-assembly (EISA) method. *Journal of Power Sources* **2024**, *621*, 235295. [Crossref]

46. Khan, M. Z.; Iltaf, A.; Ishfaq, H. A.; Khan, F. N.; Tanveer, W. H.; Song, R. H.; Mehran, M. T.; Saleem, M.; Hussain, A.; Masaud, Z.; Flat-tubular solid oxide fuel cells and stacks: a review. *Journal of Asian Ceramic Societies* **2021**, *9*, 745. [Crossref]
47. Ramkiran, A.; Vo, D. V. N.; Mahmud, M. S.; Syngas production from ethanol dry reforming using Cu-based perovskite catalysts promoted with rare earth metals. *International Journal of Hydrogen Energy* **2021**, *46*, 24845. [Crossref]
48. Deng, Y.; Li, S.; Appels, L.; Zhang, H.; Sweygers, N.; Baeyens, J.; Dewil, R.; Steam reforming of ethanol by non-noble metal catalysts.; *Renewable and Sustainable Energy Reviews* **2023**, *175*, 113184. [Crossref]
49. Boldrin, P.; Ruiz-Trejo, E.; Mermelstein, J.; Bermúdez Menéndez, J. M.; Ramírez Reina, T.; Brandon, N. P.; Strategies for Carbon and Sulfur Tolerant Solid Oxide Fuel Cell Materials, Incorporating Lessons from Heterogeneous Catalysis. *Chemical Reviews* **2016**, *116*, 13633. [Crossref]
50. Hariharan, D.; Sarkar, B.; Gundlapally, S.; Modeling and analysis of direct internal reforming in ethanol-fueled SOFC. *Emergency Management Science and Technology* **2024**, *4*, 16. [Crossref]
51. Bang, S.; Lee, J.; Lee, W.; Highly connected oxygen ion conduction pathways in anode functional layer for high performance solid oxide fuel cells. *Journal of Power Sources* **2023**, *553*, 232290. [Crossref]